

ENGINEERING

Stimuli-responsive and on-chip nanomembrane micro-rolls for enhanced macroscopic visual hydrogen detection

Borui Xu,¹ Ziao Tian,¹ Jiao Wang,^{1,2} Heetak Han,³ Taeyoon Lee,^{3*} Yongfeng Mei^{1*}

Nanomembrane rolling offers advanced three-dimensional (3D) mesostructures in electronics, optics, and biomedical applications. We demonstrate a high-density and on-chip array of rolled-up nanomembrane actuators with stimuli-responsive function based on the volume expansion of palladium in hydrogen milieu. The uniform stimuli-responsive behavior of high-density nanomembrane rolls leads to huge macroscopic visual detection with more than 50% transmittance change under optimization of micropattern design. The reversible shape changing between rolled and flat (unrolled) statuses can be well explained on the basis of the elastic mechanical model. The strain change in the palladium layer during hydrogen absorption and desorption produces a marked change in the diameter of nanomembrane rolls. We found that a functional palladium layer established an external compressive strain after hydrogen stimuli and thus also reduced the rolls' diameters. The large area of the nanomembrane roll array performs excellent nonelectrical hydrogen detection, with response and recovery speeds within seconds. Our work suggests a new strategy to integrate high-density 3D mesoscale architectures into functional devices and systems.

INTRODUCTION

Origami as a traditional art can transform flat papers into complex three-dimensional (3D) objects and inspires the fabrication of novel mesostructures by folding planar films or nanomembranes into 3D forms based on stress engineering (1, 2). Stress engineering includes internal stress (3, 4) and mechanically active (5, 6) and guided stress (7) for novel applications such as stretchable electronics (8, 9), 3D photodetectors (10), intelligent micro/nanorobots (11), active antennas (12), transformable metamaterials (13), and artificial vasculature (14). 3D structures and devices inspired by origami or kirigami (2) can save physical space for the integration density compared with planar silicon processing technology, and their large displacement/deformation feasibility by 2D free movement enables application potential in microelectromechanical systems (15), sensors, and actuators (16). Rolled-up nanotechnology is similar to the rolling of newspapers and has stimulated increasing interest in micro/nanomotors (17, 18), optical microcavities (19–21), and cell culture scaffolds (22, 23). The rolled-up tubular structures provide prominent mechanical, optical, and electrical properties that are explored and applied in the detection and sensing of gas (24), humidity (25), light (26), fluids (27), and molecules (28). Because most are static structures or devices, there is still no activated detection/sensing device or smart system to take advantage of rolling, which can overcome the bending stiffness and accommodate activated matters in a 3D fashion compared with cantilever-based actuation. Here, we adopt nanomembrane micro-rolls (NRs; that is, self-rolled-up nanomembranes) with low bending stiffness and demonstrate origami-inspired 3D rolled-type microactuators for nonelectrical visual hydrogen gas detection by combining rolled-up nanotechnology and stimuli-responsive activation. The origami-inspired 3D NRs can transform between rolled and unrolled (planar) statuses of nanomembranes due to the reversible

volume expansion of the deposited palladium (Pd) layer in a hydrogen milieu. A large-scale array of NRs-based microactuators presents excellent actuation and detection performance including more than 50% change in transmittance (enhanced color contrast), rapid response and recovery speed within several seconds, good stability, and reversibility, as well as low detection limit down to 1% hydrogen in volume ratio. Detection demonstrations based on nonelectrical visual display are put forward to give application examples of origami-inspired 3D mesostructures, which could be applied to other smart detection and actuation systems.

RESULTS

A stimuli-responsive NR array was fabricated via conventional rolled-up nanotechnology (Fig. 1, A to C). Titanium (Ti), chromium (Cr), and palladium (Pd) materials with thicknesses of 5, 5, and 20 to 50 nm, respectively, were deposited successively on a patterned photoresist layer to construct prestressed nanomembranes. All deposition was operated with glancing angle alignment to form an open etching window so that all patterned nanomembranes could achieve identical directional rolling (4). Moreover, glancing angle deposition creates a tight anchor in the opposite direction, which holds the NRs onto the substrate. After etching the photoresist layer, an NR array was achieved by stress relaxation in the nanomembrane system. Its scanning electron microscopy (SEM) image is shown in Fig. 1A. Figure 1B shows a large-scale optical image of a high-density stimuli-responsive NR array, which comprises a functional area of 5 mm × 5 mm on a glass substrate, as shown in Fig. 1C. The almost 100% yield in our NR array fabrication is very crucial for further visual detection. The processing key is the quality control and deposition conditions of nanomembranes, which should guarantee the nanomembrane uniformity in all parameters such as thickness, density, and conformity. For instance, to obtain NRs with high density and excellent uniformity, evaporation distance length between the target source and the substrate was adjusted to ensure the materials were deposited onto the substrates with ultimately equal nanomembrane thickness and built-in prestrain, although it is limited by the deposition methods.

¹Department of Materials Science, State Key Laboratory of ASIC and Systems, Fudan University, Shanghai 200433, China. ²School of Information Science and Engineering, Fudan University, Shanghai 200433, China. ³Nanobio Device Laboratory, School of Electrical and Electronic Engineering, Yonsei University, Seoul 120749, Republic of Korea.

*Corresponding author. Email: yfm@fudan.edu.cn (Y.M.); taeyoon.lee@yonsei.ac.kr (T.L.)

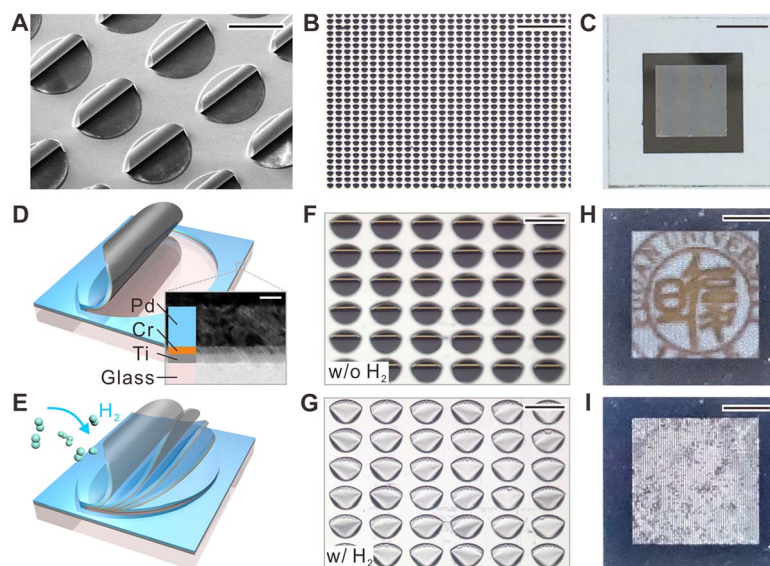


Fig. 1. Configuration and stimuli-responsive performance of high-density stimuli-responsive NRs. (A) SEM images depicting the structure of NRs. Scale bar, 50 μm . (B) Optical image depicting the successful fabrication of NRs with high density. Scale bar, 500 μm . (C) Photograph of 5.5-mm \times 5.5-mm array of NRs on a glass substrate. The light gray part is NRs, whereas the dark gray part is the planar nanomembrane as a contrast. Scale bar, 4 mm. (D) Scheme depicting the configuration of NR. The inset is the cross-section TEM image of the deposited trilayer nanomembrane system consisting of Ti, Cr, and Pd from the bottom up. Scale bar, 25 nm. (E) Scheme depicting stimuli-responsive behavior of NR. The NRs change from tubular structure into planar status with hydrogen stimuli. (F and G) Optical images depicting the NR array responding to hydrogen stimuli. Scale bars, 100 μm . (H and I) Visual images depicting the NR array responding to hydrogen stimuli. Scale bars, 2 mm.

NR-based actuators are composed of Ti, Cr, and Pd layers on a glass substrate, where Ti/Cr layers serve as a strained layer (29) and the Pd layer serves as a stimuli-responsive layer, as sketched in Fig. 1D. The structure of the trilayer nanomembrane was confirmed, as shown in the inset of Fig. 1D. The transmission electron microscopy (TEM) image shows that the total thickness of this trilayer nanomembrane is 60 nm, and their components are further checked in fig. S1. Rolling of the nanomembrane with a total thickness of 30 to 60 nm corresponds to a low bending stiffness value D ($D = Et^3/12$, where E is the Young's modulus and t is the film thickness) in the order of 10^{-12} N·m, which is comparable to polydimethylsiloxane with a thickness of several micrometers (30) and ensures the rolling actuation behavior upon stimulation. The stimuli-responsive property takes advantage of marked volume expansion of Pd materials during hydrogen absorption (31), as schematically shown in Fig. 1E. The volume change caused by phase transition of Pd from PdH_α to PdH_β (31) enables the stimuli-responsive NR to return to a planar state (Fig. 1G) from the rolled shape (Fig. 1F), as shown in movie S1. Movie S1 shows the stimuli-responsive behavior of a typical NR array. All NRs present a highly uniform stimuli-responsive behavior and transformation between rolls and the planar nanomembrane simultaneously. Meanwhile, this behavior was not evident without the Pd functional layer (fig. S2). As shown in Fig. 1F, Janus-shaped nanomembranes designed with a large section and a small semicircle form into NRs and leave the empty area as the dark color due to the prestress once released from the substrate (noted as without H_2). Upon the stimuli of hydrogen, NRs become unrolled (planar) with certain wrinkles due to Pd volume change (Fig. 1G). Their wrinkled shapes could be attributed to the average compressive strain in the whole nanomembrane (32). Because hydrogen stimuli are applied to NRs, the Pd layer tends to expand itself. However, the upper part of the nanomembrane is confined by the anchor, which is made by glancing angle deposition. Thus, external confinement prevents the expansion of the nanomembrane, generating an external compressive stress. Cendula *et al.* (32) elucidate that only an av-

erage compressive strain could generate wrinkles on the nanomembrane. The fabricated device comprising the NR arrays is semitransparent so that the image of the Fudan logo underneath the sample is observable (as shown in Fig. 1H) due to the empty area left from rolling. With hydrogen stimuli, NRs transform to planar structures covering the empty area, which leads to the opaque status with the nanomembrane color (Fig. 1I). The NRs with high yield and their uniform stimuli-responsive behavior ensure the feasibility of amplifying the stimuli-responsive behavior into macroscale color contrast, which is observable with the naked eye.

To enhance visual contrast, we investigated high-yield stimuli-responsive NRs with different photoresist pattern parameters, as shown in Fig. 2. The area ratio is defined as the ratio of the transparent area to the total area, which will decide the transmittance of NRs. The ideal change of the area ratio with hydrogen stimuli is influenced by the shape of the photoresist pattern, arrangement mode, and density (L/λ), where L is the length of the pattern and λ is the periodicity of ordered patterns, as depicted in the right panels of Fig. 2. First, we calculated the area ratio change of each panel in different densities (lines in Fig. 2), and plotted the experimental results according to the corresponding pattern design and arrangement. The circle pattern is shown with circle spots, whereas another Janus pattern is shown with semicolored spots in different shapes. The area ratio change of NRs fabricated in a circle pattern (dark line in Fig. 2) is the lowest because only half of the nanomembrane is free to vary with hydrogen stimuli. Basically, the largest one can be obtained by a rectangular or square pattern. However, only one straight side connection with the substrate makes it fragile during the transformation process, and hence, the soft nanomembrane is easily detached from the substrate when it transforms between rolling and unrolling, especially after the high-concentration hydrogen stimuli (fig. S3). To balance the stability and visual contrast, a Janus pattern consisting of a semicircle and section was applied to increase the area ratio change to 1.41 times compared with a circle in the same density (red line in Fig. 2), but high yield and stability were kept. Likewise, the

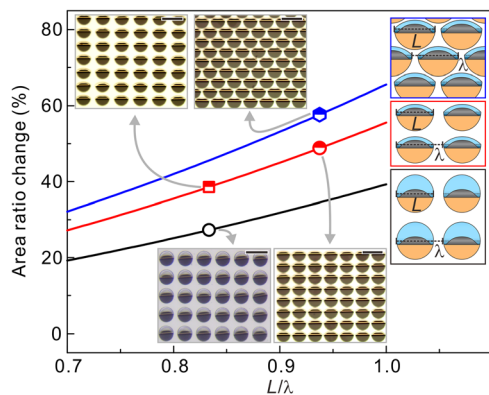


Fig. 2. Area ratio change of NRs related to L/λ for different pattern designs and arrangements. The area ratio is defined as the ratio of the transparent area to the total area. L is the diameter of the circle pattern and semicircle part of the Janus pattern. λ is periodicity. Lines are the calculated results, as shown in the right panels. Black line, circle patterns in square arrangement; red line, Janus patterns in rectangular arrangement; blue line, Janus patterns in hexagonal arrangement. Insets of optical images depict successful fabrication of large arrays of NRs with patterns corresponding to the dots in the diagram. Scale bars, 100 μm .

area ratio change can be further enlarged by creating higher density, once we guarantee the yield of uniform fabrication of NRs. Patterns arranged in a rectangular array have a periodicity of 90 μm with a 75- μm -diameter pattern ($L/\lambda = 75/90 = 0.83$, red square and corresponding inset in Fig. 2). For these 4560 NRs on a 5.5-mm \times 5.5-mm substrate, the density and area ratio change of this array are calculated to be 15,000 cm^{-2} and 38.56%, respectively. If we shorten the periodicity to 80 μm ($L/\lambda = 75/80 = 0.94$, red circle and corresponding inset in Fig. 2), then we can place 6392 NRs in the same area, and the density and area ratio change increase to 21,130 cm^{-2} and 48.81%, respectively. When the pattern is rearranged more efficiently in a hexagonal array (blue hexagon and corresponding inset in Fig. 2), the density of NRs increases to 24,324 cm^{-2} with 57.67% area ratio change. The maximum density and area ratio change are calculated if we set $L/\lambda = 1$ in a hexagonal array, that is, the density reaches 29,020 cm^{-2} and the area ratio change is 65.61%. In this manner, we successfully integrated NRs into a high-density array to enhance the visual contrast.

The area ratio change is also influenced by the curvature of NRs. After hydrogen stimuli, there is a decrease in the diameter of NRs with various concentrations $[\text{C}(\text{H}_2)]$, as shown in Fig. 3A and fig. S4. This behavior creates a higher area ratio change by decreasing the diameter of NRs and peeling off more parts of the nanomembrane, which are influenced by hydrogen concentration. Higher concentration leads to a smaller diameter (from left to right in Fig. 3A), and more parts of the nanomembrane rolling. This is attributed to the external compressive strain in the Pd layer after hydrogen stimuli (33). To clarify this phenomenon, a calculation based on elastic mechanics (32, 34, 35) was carried out, as shown in Fig. 3B. According to the calculated curves, with a given strain in the Ti and Cr layers, the diameter of NMRs shows a positive correlation with the Pd internal strain. The experimental results are plotted on the curves according to the measured diameters. The results reflect that after hydrogen stimuli, the internal strain of the Pd layer decreases, resulting in smaller diameters, and the higher concentration of hydrogen leads to a smaller internal strain in the Pd layer. The influence of the Pd layer thickness (20, 30, 40, and 50 nm with black, red, blue, and magenta, respectively) is also shown in Fig. 3B. Generally speaking, the thicker the nanomembrane is, the larger the di-

ameter of the resulting roll. However, as observed in Fig. 3, the fabricated NRs present different internal strains in the Pd layer, which could be influenced by the deposition thickness (33) and conditions (36), and this difference leads to the phenomenon of the diameter of the 20-nm Pd sample being much larger than the diameters of the other samples.

To illustrate the stimuli-responsive behavior of NRs, we performed a typical responsive process of a single NR deposited with the 20-nm Pd layer in hydrogen milieu, as shown in Fig. 4A. The curvature above zero in the y axis corresponds to the upward bending (for example, rolling), whereas the area ratio in the y axis is applied to elucidate the downward-bending status because of the difficulty in measuring the curvature. The larger ratio refers to the larger curvature. As for the zero point, it stands for the issue of an ideal planar nanomembrane, where the curvature is zero and the transparent area is fully covered by unrolled nanomembranes. The light blue region in Fig. 4A is the period in which the NR is under 2% hydrogen stimuli, whereas other regions describe the behavior of the sample before or after stimuli. With hydrogen stimuli, the curvature of the NR rapidly decreases close to zero, and then the nanomembrane bends slightly downward (0 to 20 s). Rather than rolling into a single tube, it prefers bending downward from two directions (20 s), and a few wrinkles are also observed simultaneously near the anchor part, where the increased internal strain could not be relaxed via bending. This phenomenon is attributed to an average compressive strain status in the nanomembrane system (32). When the stimuli are removed, the stimuli-responsive NR operates inversely, the wrinkle disappears, and the nanomembrane returns to a flat status at 36 s. Then, the NR rolls into a smaller microtube (40 s) ready for the next hydrogen stimuli. The curvature does not change immediately as hydrogen stimuli are applied, especially at a low concentration of hydrogen (fig. S5). This delayed behavior is attributed to the fact that hydrogen atoms enter the preexisting microstructural defects without lattice expansion at the beginning of hydrogen absorption (37).

The mechanism of the stimuli-responsive behavior of the NR was elucidated by analytical calculation of the relationship between the diameter of the NR and the Pd layer strain property, which is shown in Fig. 4B and fig. S6. The diameter of the fabricated NRs is ca. 20 μm (according to Fig. 3), corresponding to ca. 0.5% tensile strain in the Pd layer, which is located in the sharp slope area of the curve. The internal strain in the Pd layer was further confirmed by x-ray diffraction (XRD), in which the fabricated Pd generates 0.5% lattice mismatch compared with the relaxed Pd lattice (fig. S7). With hydrogen atoms diffusing into Pd lattices, the tensile strain in Pd increases due to the formation of PdH_x , leading to a larger strain. With more hydrogen absorption, the phase PdH_β is formed, generating more tensile strain. Therefore, the NR changes into planar (unrolled, gray area in Fig. 4B) structures and reversely bent with the increasing tensile strain (magenta line in Fig. 4B). The tensile strain lessens with the desorption of hydrogen, so the nanomembrane system rolls upward again. As shown in fig. S6, the curvature of the thinner nanomembrane is more sensitive to the strain change because of lower bending stiffness. This sensitive response to strain change is expected to increase the response speed to hydrogen (which will be discussed later). The insets in Fig. 4B show our simulation by finite element method (FEM) of rolled-up nanomembranes with the 20-nm Pd layer. The gray line depicts the original shape of the nanomembrane. With a given internal strain, the nanomembrane bends upward and forms a bending microstructure (inset a in Fig. 4B). To simulate the nanomembrane under hydrogen stimuli, the strain in the Pd layer was increased slightly (0.2%) and the nanomembrane went into the unbent status (inset b in Fig. 4B). As the strain increases to 0.5%,

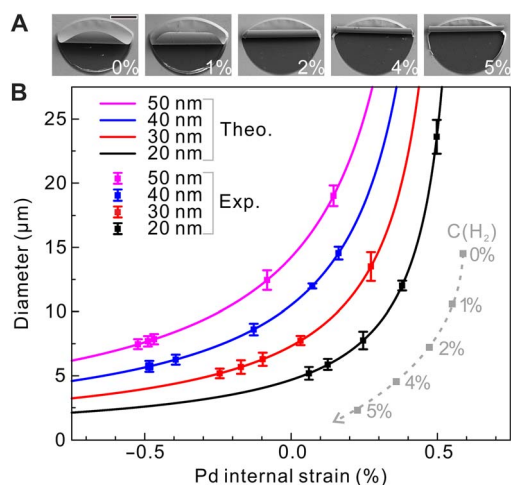


Fig. 3. Diameter-decreasing behavior of NR after hydrogen stimuli. (A) SEM images depicting the decreased diameter of NR after different concentration hydrogen stimuli. Scale bar, 25 μm . (B) Diameter of NRs related to the Pd internal strain change after hydrogen stimuli. The experimental results were plotted in the diagram according to the diameter after hydrogen stimuli of different concentrations.

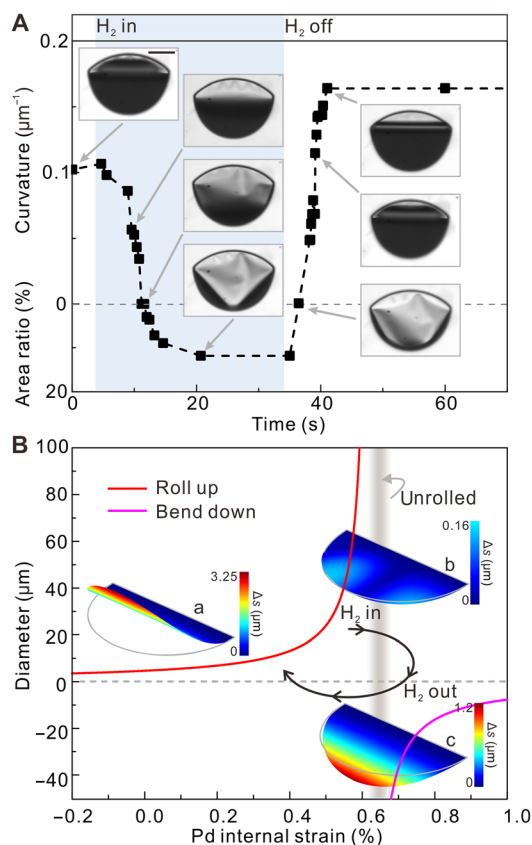


Fig. 4. Stimuli-responsive behavior of single NR. (A) Diagram depicting NR change with and without 2% hydrogen stimuli. Insets are the optical images of the hydrogen stimuli-responsive behavior. Scale bar, 25 μm . (B) Analytical calculation of NR diameter related to the internal strain. The insets show FEM simulation results of NRs with predefined strain (inset a) and increased strain in the Pd layer after hydrogen injection (lesser strain in inset b and higher strain in inset c). Color reflects the distribution of displacement (Δs).

the nanomembrane bends downward (inset c in Fig. 4B). With the desorption of hydrogen, the applied external tensile strain is removed and the nanomembrane rolls back to its original status (inset a in Fig. 4B). Hence, one cycle of hydrogen in and out is completed, as shown in the insets (from inset a to inset b to inset c and then back to inset a). It is intriguing that the small tensile strain can induce huge deformation of the NR, especially with a thinner nanomembrane. With the formation of PdH_β , hydrogen-induced lattice expansion can reach as high as 3.5%. However, this phase transition only occurs in the hydrogen environment with a concentration of more than 1.5% (38), which restricts the detection limit of mechanical-based hydrogen detectors. According to the analytical calculation and simulation, our NR requires little strain variation to realize the change between rolled and planar statuses. We actually observed that it can respond to 1% hydrogen stimuli (black line in fig. S5) beyond the phase transition limit.

Furthermore, we quantitatively examine the visual detection effect of a large array of stimuli-responsive NRs. To measure the transmittance difference quantitatively, we reported the transmittance spectra of high-density NRs in the first hydrogen stimuli cycle, as shown in Fig. 5A. The testing chamber with hydrogen gas inlet and outlet was placed in an ultraviolet-visible (UV-vis) spectrophotometer to measure the transmittance (schematic inset in Fig. 5A). The transmittance in the measured range was kept constant, which is in agreement with the gray color observed in Fig. 1C. The original transmittance is around 32% in the whole measure wavelength range (350 to 700 nm). With the injection of 4% hydrogen, the transmittance drops down to 17% due to unrolled nanomembranes, recovers after hydrogen stimuli, and rises to a higher level due to the smaller tubular structures, as shown in Fig. 3. Thus, transmittance change exceeding 50% is obtained during the response process, which is enough for observation with the naked eye. Therefore, visual hydrogen detection application based on a large array of stimuli-responsive NRs is demonstrated, as shown in insets b and c of Fig. 5A (as captures of movie S2). The array of NRs was designed in a 2.3-cm \times 0.6-cm pattern with specific characters “FUDAN.” Under sunlight irradiation, reversible color change occurs as a result of the rolling and unrolling transformation. Not only does the color change occur, but the reflection of sunlight is also noticeable during the application and removal of the stimuli (movie S2). The reflection variation provides a clearer signal than transmittance. Because of the uniform stimuli-responsive behavior of the NR array, it is believed that the dynamic color change reveals the responding sequence of an individual device upon flowing hydrogen on its surface.

The detection properties of nonelectrical visual hydrogen detectors are shown in Fig. 5B. This dynamic test was applied to present the first stimuli-responding cycle of different samples with different hydrogen stimuli. The dynamic curves of transmittance present similar trends with a single NR change in Fig. 4A, confirming the uniform responsive behavior of thousands of stimuli-responsive NRs. In high hydrogen concentration stimuli (more than 4%), all samples operate with the same stimuli-responsive process as follows: With hydrogen injection, the transmittance decreases rapidly due to the reduction of the curvature of NRs until the curvature changes to zero. Then, a slight increase happens as a result of the downward bending, increasing the area ratio. Finally, the transmittance reaches a balanced level. When the hydrogen desorption happens, the transmittance drops down first and then rises with the reverse bending behavior of NRs, and the increase of transmittance ends up at a higher level because of the smaller tube. In the low-concentration environment, the volume expansion of Pd cannot provide tensile strain similar to that in the high concentration. In the 2% hydrogen

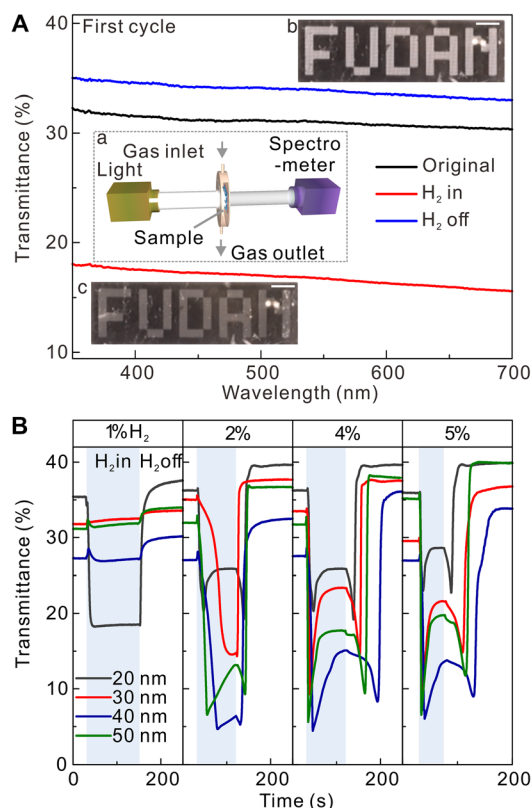


Fig. 5. Detection property of a high-density NR array as hydrogen detectors. (A) Transmittance spectra of high-density NRs before (original), during (H_2 in), and after hydrogen stimuli (H_2 out). The testing sample is with the 50-nm Pd layer. Inset a is the scheme of the testing system for transmittance measurement of NRs. Insets b and c are the real images depicting the visual change of FUDAN characters composed of high-density NRs without (b) and with (c) hydrogen stimuli. Scale bars, 2 mm. (B) Time-dependent transmittance spectra of high-density NRs with different Pd layer thicknesses and different concentration hydrogen stimuli.

environment, where the phase transition of Pd can occur, we still notice the increase in transmittance as a result of reverse bending. However, the speed of transmittance change is much slower. For the 30-nm Pd sample, transmittance does not increase because the increase in the tensile strain cannot afford reverse bending. As for the lower concentration, with 1% hydrogen stimuli, an obvious transmittance change is observed in the stimuli-responsive NR with a thinner Pd layer (20 nm thickness). A small internal strain change without phase transition can still offer enough driving force for thinner nanomembrane bending, which hints that thinner nanomembranes could offer more flexible actuation due to their low bending stiffness.

The results of the dynamic test are shown in Fig. 5B, and the response and recovery time of the stimuli-responsive NR-based hydrogen detector are listed in Table 1. Response and recovery time are defined as the time required to reach down to or up to, respectively, 90% of the difference between the transmittance without hydrogen and stable transmittance in hydrogen. It is encouraging that 3.4 and 7.6 s are needed, respectively, for our fastest response and recovery time, which are considerable speeds for commercial applications (39). The 20-nm Pd layer sample can detect down to 1% hydrogen in volume, breaking the limitation of the traditional mechanical hydrogen detector based on the phase transition effect. The response time speeds up with higher concentrations of hydrogen as a consequence of faster phase transition,

Table 1. Response and recovery time of NR-based hydrogen detectors upon exposure in various hydrogen concentrations. N/A, not available.

Thickness (nm)	Response time (s)				Recovery time (s)			
	1%	2%	4%	5%	1%	2%	4%	5%
20	9	8	8	3.4	18.6	28.8	29.2	24.4
30	N/A	61.6	7.2	3.6	N/A	7.6	36.6	53.2
40	N/A	44.2	12.2	7.6	N/A	27.2	64.2	81.2
50	N/A	20	4.7	3.4	N/A	26.4	51	47.4

whereas recovery time increases for longer desorption time. Besides, both response and recovery time were longer for the thicker Pd layer, which we attribute to higher bending stiffness. However, the response time of 50-nm Pd layer NRs is much shorter than that of the thinner layers. The reason behind this phenomenon is that the thick nanomembrane system rolls into a curved structure instead of a tube so that the NR responds faster once the hydrogen atoms are injected into the Pd lattice. The dynamic analysis of transmittance shows that NRs with a thinner Pd layer are suitable for sensitive detection. On the other hand, NRs with a thicker Pd layer perform better in higher concentrations due to high speed and enhanced contrast.

Stability was also tested, as shown in fig. S8, with 4% hydrogen stimuli in a cycle of 90 s on-state and 120 s off-state. The NR array performed very well after 30 cycles, and the rolls became slightly smaller, as shown in fig. S9 and Fig. 3B. Such good stability proves that nanomembrane rolls could tolerate a large volume change (40) due to their low bending stiffness. Note that the response and recovery time are slightly longer after several cycles of hydrogen stimuli (fig. S10), which could be attributed to the smaller tube formed after hydrogen stimuli (fig. S9). A smaller tube needs more time to overcome the friction and open the NR.

DISCUSSION

In summary, on-chip stimuli-responsive NR arrays were successfully fabricated in high yield via conventional photolithography and a wet lift-off procedure, which are compatible with the planar fabrication process. The NRs respond to hydrogen stimuli by changing from rolled to planar statuses based on the volume expansion of the Pd inner layer in a hydrogen environment. With optimal design of pattern, more than $24,000 \text{ cm}^{-2}$ NRs were integrated on the transparent substrate, resulting in more than 50% transmittance change, which is observable with the naked eye. Reversible shape changing is elucidated by elastic mechanical calculation and finite element analysis simulation, owing to the strain change in the Pd layer with and without hydrogen stimuli. The strain change after hydrogen stimuli also leads to an obvious decrease of the diameter of the NR. We demonstrate nonelectrical hydrogen detection based on the high-density array of NRs, which shows surrounding hydrogen via noticeable color change with a response time of 3.4 s and a recovery time of 7.6 s. Optimization in the Pd layer thickness lowers the detection limit down to 1% hydrogen. The high-density stimuli-responsive NRs pave the way to integrate stress-induced 3D mesostructures to realize macroscopic devices or systems without complex assistance.

MATERIALS AND METHODS

Fabrication of stimuli-responsive NR

A positive photoresist (AR-P 3510T, Allresist GmbH) was first spin-coated on a clean glass or quartz substrate. The photoresist pattern arrays with different sizes and shapes were fabricated with an optical direct laser writing lithography system (μ PG501, Heidelberg Instruments). Metal layers including titanium (Ti), chromium (Cr), and palladium (Pd) were subsequently deposited by e-beam evaporation (TSV700, Tenstar Vacuum) with a glancing angle of 60°. The thicknesses of Ti and Cr were controlled as 5 nm. Meanwhile, the Pd thickness was tuned from 20 to 50 nm. The deposition rate of these three layers was controlled at 1.0 Å/s. After deposition, samples were immersed in acetone to remove the photoresist and then dried with a critical point dryer (Autosamdri-815B, Tousimis) to prevent the sample from collapsing during liquid evaporation.

Characterization of morphology and stimuli-responsive behavior

The morphology of NRs was observed with a scanning electron microscope (SIGMA Field Emission SEM, Zeiss). The cross-section structure of NMRs was obtained with a high-resolution transmission electron microscope (Tecnai G² F20 S-TWIN, FEI), and the component was examined by energy-dispersive x-ray spectroscopy. To obtain images of the stimuli-responsive behavior, the sample was first put in a transparent polymethyl methacrylate (PMMA) chamber with gas inlet and outlet. Hydrogen mixture with nitrogen in a certain concentration and pure nitrogen were injected into the chamber separately to trigger the responsive behavior. At the same time, the shape changing of NMRs was observed with an optical microscope (BX51, Olympus) and recorded with a camera (FR180, NorPix) at 30 frames per second.

Transmittance characterization

The self-designed system for transmittance measurement is shown in the inset of Fig. 5A. A 5.5-mm \times 5.5-mm array of the NR was placed in a PMMA chamber with a testing glass window. The hydrogen mixture was injected into the chamber through a flowmeter so that the flow rate could be tuned to 100 sccm (standard cubic centimeters per minute). The chamber was put inside a UV-vis spectrophotometer (UV-2550, Shimadzu) to collect data. Two different measurements were carried out, including spectrum scanning and dynamic analysis. The scanning range was from 350 to 700 nm, and 580-nm incident light was applied for dynamic analysis.

Area ratio change and density calculation

Because the area ratio is defined as the ratio of the transparent area to the total area, we simplified the model to calculate the area ratio change as follows. We assumed that when the nanomembrane changes into the planar status, the transparent area is totally covered. Therefore, the area ratio change with hydrogen stimuli is equal to the original area ratio. In addition, the area covered by the rolled-up nanomembrane is ignored.

For circle patterns with length L and periodicity λ (black panel in Fig. 2), the area ratio change is calculated as

$$R_{ac} = \frac{(\pi L^2)/8}{\lambda^2} = \frac{\pi}{8} \left(\frac{L}{\lambda}\right)^2$$

For Janus patterns in rectangular arrangement (red panel in Fig. 2), the area ratio change is calculated as

$$R_{ac} = \frac{(\pi L^2)/8}{\lambda^2/\sqrt{2}} = \frac{\sqrt{2}\pi}{8} \left(\frac{L}{\lambda}\right)^2$$

For Janus patterns in hexagonal arrangement (blue panel in Fig. 2), the area ratio change is calculated as

$$R_{ac} = \frac{(\pi L^2)/8}{\lambda^2 \times (\sqrt{2} + 2\sqrt{2} - 1)/2} = \frac{\pi}{4(\sqrt{2} + 2\sqrt{2} - 1)} \left(\frac{L}{\lambda}\right)^2$$

The density of arrays is

$$D = \frac{R_{ac}}{(\pi L^2)/8} \times 10^8 \text{ cm}^{-2}$$

Analytical calculation and simulation

The model was established on the basis of the elastic calculation of the plane strain assumption, which is suitable to the nanomembrane rolling from one direction (32, 34, 35). The parameters used in this model include thickness t_i , Young's modulus E_i , Poisson's ratio ν_i , and initial strain ϵ_i^0 of the layer i .

We can obtain the general parameters and the radius of a three-layer system ($i = 1, 2, 3$, corresponding to the Ti, Cr, and Pd layer, respectively) as follows

$$y_0 = 0, y_1 = t_1, y_2 = t_2 + t_1, y_3 = t_3 + t_2 + t_1$$

In the plane strain assumption, we obtain

$$E'_i = \frac{E_i}{1 - \nu_i^2}, \quad \eta_i = 1 + \nu_i$$

$$c = \frac{\sum_{i=1}^3 E'_i t_i \eta_i \epsilon_i^0}{\sum_{i=1}^3 E'_i t_i}, \quad y_b = \frac{\sum_{i=1}^3 E'_i t_i (y_i + y_{i-1})}{2 \sum_{i=1}^3 E'_i t_i}$$

Thus

$$\text{Radius} = \frac{3 \sum_{i=1}^3 E'_i t_i (y_i + y_{i-1} - 2y_b)(c - \eta_i \epsilon_i^0)}{2 \sum_{i=1}^3 E'_i t_i [y_i^2 + y_{i-1} y_i + y_{i-1}^2 - 3y_b (y_i + y_{i-1} - y_b)]}$$

To rationalize our calculation results, the strain in Ti, Cr, and Pd was estimated and measured. First, we fabricated the Ti/Cr bilayer, in which the thickness was tuned to 5 nm. According to the formula above and the measured diameter of the Ti/Cr NR (fig. S11), the strain gradient between Ti and Cr was estimated to be 0.5%. Then, the strain in the 20-nm Pd layer was confirmed by XRD (fig. S7), calculated to be 1.0%. Finally, the internal strain in each layer was calculated on the basis of the measured diameter of the fabricated NR with the 20-nm Pd layer. Therefore, the strain in each layer was set at 1.0, 0.5, and 0.5% for this sample.

The model used for simulation is simplified as a semicircle nanomembrane with a radius of 5 μm , which is much smaller compared with the real photoresist pattern size but enough to illustrate the phenomenon. The elastic parameters of materials as E_i and ν_i are the same as those in analytical calculation. The thickness of layers 1, 2, and 3 is 5, 5 and 20 nm, respectively. The initial strain for bending is tuned as 1.0, 0.5, and 0.5% isotropic strain for layers 1, 2, and 3, respectively. After that, an increase of initial strain in layer 3 is applied to simulate the stimuli-responsive process, which is set as 0.2 and 0.5%. In this manner, we obtained the simulation results of the initial bending state of the NR without hydrogen and the balanced morphology in a hydrogen atmosphere.

SUPPLEMENTARY MATERIALS

Supplementary material for this article is available at <http://advances.sciencemag.org/cgi/content/full/4/4/eaap8203/DC1>

Pattern size regulation of stimuli-responsive NRs

fig. S1. The energy-dispersive x-ray spectrum of nanomembrane consisting of Ti, Cr, and Pd.

fig. S2. Hydrogen influence on NRs consisting of Ti/Cr bilayer.

fig. S3. The optical images depicting NRs in square pattern design.

fig. S4. SEM images of NR's diameter decreasing after different concentration hydrogen stimuli.

fig. S5. Stimuli-responsive behavior in different hydrogen environments (1 to 5%).

fig. S6. Analytical calculation of NR's curvatures as a function of internal strain and thickness of Pd layer.

fig. S7. XRD pattern of nanomembrane consisting of Ti, Cr, and Pd.

fig. S8. Cycling performance of hydrogen detection in hydrogen environment of 4% concentration.

fig. S9. Optical images of NRs before the test and after 20 and 30 cycles of 4% hydrogen stimuli.

fig. S10. Stimuli-responsive behavior related to the stimuli cycle times.

fig. S11. Optical image of fabricated Ti/Cr NR.

fig. S12. Visual effects of high-density NRs with different pattern diameters of 50 μm (left), 75 μm (center), and 100 μm (right).

fig. S13. Stimuli-responsive behavior of single NR in different diameters of pattern.

movie S1. Stimuli-responsive behavior with 2% hydrogen.

movie S2. The change of FUDAN pattern NRs with 4% hydrogen under sunlight.

REFERENCES AND NOTES

- F. Cavallo, M. G. Lagally, Nano-origami: Art and function. *Nano Today* **10**, 538–541 (2015).
- J. Rogers, Y. Huang, O. G. Schmidt, D. H. Gracias, Origami MEMS and NEMS. *MRS Bull.* **41**, 123–129 (2016).
- O. G. Schmidt, K. Eberl, Nanotechnology: Thin solid films roll up into nanotubes. *Nature* **410**, 168 (2001).
- Y. Mei, G. Huang, A. A. Solovev, E. B. Ureña, I. Mönch, F. Ding, T. Reindl, R. K. Y. Fu, P. K. Chu, O. G. Schmidt, Versatile approach for integrative and functionalized tubes by strain engineering of nanomembranes on polymers. *Adv. Mater.* **20**, 4085–4090 (2008).
- J.-H. Cho, T. James, D. H. Gracias, Curving nanostructures using extrinsic stress. *Adv. Mater.* **22**, 2320–2324 (2010).
- E. Hawkes, B. An, N. M. Benbernou, H. Tanaka, S. Kim, E. D. Demaine, D. Rus, R. J. Wood, Programmable matter by folding. *Proc. Natl. Acad. Sci. U.S.A.* **107**, 12441–12445 (2010).
- S. Xu, Z. Yan, K.-I. Jang, W. Huang, H. Fu, J. Kim, Z. Wei, M. Flavin, J. McCracken, R. Wang, A. Badea, Y. Liu, D. Xiao, G. Zhou, J. Lee, H. U. Chung, H. Cheng, W. Ren, A. Banks, X. Li, U. Paik, R. G. Nuzzo, Y. Huang, Y. Zhang, J. A. Rogers, Assembly of micro/nanomaterials into complex, three-dimensional architectures by compressive buckling. *Science* **347**, 154–159 (2015).
- D.-Y. Khang, H. Jiang, Y. Huang, J. A. Rogers, A stretchable form of single-crystal silicon for high-performance electronics on rubber substrates. *Science* **311**, 208–212 (2006).
- J. A. Rogers, T. Someya, Y. Huang, Materials and mechanics for stretchable electronics. *Science* **327**, 1603–1607 (2010).
- H. C. Ko, M. P. Stoykovich, J. Song, V. Malyarchuk, W. M. Choi, C.-J. Yu, J. B. I. Geddes III, J. Xiao, S. Wang, Y. Huang, J. A. Rogers, A hemispherical electronic eye camera based on compressible silicon optoelectronics. *Nature* **454**, 748–753 (2008).
- K. Malachowski, J. Breger, H. R. Kwag, M. O. Wang, J. P. Fisher, F. M. Selaru, D. H. Gracias, Stimuli-responsive theragripers for chemomechanical controlled release. *Angew. Chem. Int. Ed. Engl.* **53**, 8045–8049 (2014).
- D. D. Karnaushenko, D. Karnaushenko, D. Makarov, O. G. Schmidt, Compact helical antenna for smart implant applications. *NPG Asia Mater.* **7**, e188 (2015).
- J. L. Silverberg, A. A. Evans, L. McLeod, R. C. Hayward, T. Hull, C. D. Santangelo, I. Cohen, Using origami design principles to fold reprogrammable mechanical metamaterials. *Science* **345**, 647–650 (2014).
- R. Arayanarakool, A. K. Meyer, L. Helbig, S. Sanchez, O. G. Schmidt, Tailoring three-dimensional architectures by rolled-up nanotechnology for mimicking microvasculatures. *Lab Chip* **15**, 2981–2989 (2015).
- R. J. Wood, The challenge of manufacturing between macro and micro. *Am. Sci.* **102**, 124–131 (2014).
- L. Hines, K. Petersen, G. Z. Lum, M. Sitti, Soft actuators for small-scale robotics. *Adv. Mater.* **29**, 1603483 (2016).
- A. A. Solovev, Y. Mei, E. Bermúdez Ureña, G. Huang, O. G. Schmidt, Catalytic microtubular jet engines self-propelled by accumulated gas bubbles. *Small* **5**, 1688–1692 (2009).
- V. Magdanz, G. Stoychev, L. Ionov, S. Sanchez, O. G. Schmidt, Stimuli-responsive microjets with reconfigurable shape. *Angew. Chem. Int. Ed. Engl.* **53**, 2673–2677 (2014).
- X. Li, Self-rolled-up microtube ring resonators: A review of geometrical and resonant properties. *Adv. Opt. Photonics* **3**, 366–387 (2011).
- J. Wang, T. Zhan, G. Huang, P. K. Chu, Y. Mei, Optical microcavities with tubular geometry: Properties and applications. *Laser Photon. Rev.* **8**, 521–547 (2014).
- X. Lin, Y. Fang, L. Zhu, J. Zhang, G. Huang, J. Wang, Y. Mei, Self-rolling of oxide nanomembranes and resonance coupling in tubular optical microcavity. *Adv. Opt. Mater.* **4**, 936–942 (2016).
- G. Huang, Y. Mei, D. J. Thurmer, E. Coric, O. G. Schmidt, Rolled-up transparent microtubes as two-dimensionally confined culture scaffolds of individual yeast cells. *Lab Chip* **9**, 263–268 (2009).
- W. Xi, C. K. Schmidt, S. Sanchez, D. H. Gracias, R. E. Carazo-Salas, R. Butler, N. Lawrence, S. P. Jackson, O. G. Schmidt, Molecular insights into division of single human cancer cells in on-chip transparent microtubes. *ACS Nano* **10**, 5835–5846 (2016).
- A. R. Jallil, H. Chang, V. K. Bandari, P. Robaschik, J. Zhang, P. F. Siles, G. Li, D. Bürger, D. Grimm, X. Liu, G. Salvan, D. R. T. Zahn, F. Zhu, H. Wang, D. Yan, O. G. Schmidt, Fully integrated organic nanocrystal diode as high performance room temperature NO₂ sensor. *Adv. Mater.* **28**, 2971–2977 (2016).
- J. Zhang, J. Zhong, Y. F. Fang, J. Wang, G. S. Huang, X. G. Cui, Y. F. Mei, Roll up polymer/oxide/polymer nanomembranes as a hybrid optical microcavity for humidity sensing. *Nanoscale* **6**, 13646–13650 (2014).
- H. Wang, H. Zhen, S. Li, Y. Jing, G. Huang, Y. Mei, W. Lu, Self-rolling and light-trapping in flexible quantum well-embedded nanomembranes for wide-angle infrared photodetectors. *Sci. Adv.* **2**, e1600027 (2016).
- C. S. Martinez-Cisneros, S. Sanchez, W. Xi, O. G. Schmidt, Ultracompact three-dimensional tubular conductivity microsensors for ionic and biosensing applications. *Nano Lett.* **14**, 2219–2224 (2014).
- M. Medina-Sánchez, B. Ibarlucea, N. Pérez, D. D. Karnaushenko, S. M. Weiz, L. Baraban, G. Cuniberti, O. G. Schmidt, High-performance three-dimensional tubular nanomembrane sensor for DNA detection. *Nano Lett.* **16**, 4288–4296 (2016).
- Z. Liu, J. Li, J. Wang, G. Huang, R. Liu, Y. Mei, Small-scale heat detection using catalytic microengines irradiated by laser. *Nanoscale* **5**, 1345–1352 (2013).
- Z. Wang, A. A. Volinsky, N. D. Gallant, Crosslinking effect on polydimethylsiloxane elastic modulus measured by custom-built compression instrument. *J. Appl. Polym. Sci.* **131**, 41050 (2014).
- T. B. Flanagan, W. A. Oates, The palladium-hydrogen system. *Annu. Rev. Mater. Sci.* **21**, 269–304 (1991).
- P. Cendula, S. Kiravittaya, Y. F. Mei, C. Deneke, O. G. Schmidt, Bending and wrinkling as competing relaxation pathways for strained free-hanging films. *Phys. Rev. B* **79**, 085429 (2009).
- S. Wagner, T. Kramer, H. Uchida, P. Dobron, J. Cizek, A. Pundt, Mechanical stress and stress release channels in 10–350 nm palladium hydrogen thin films with different microstructures. *Acta Mater.* **114**, 116–125 (2016).
- G. P. Nikishkov, Curvature estimation for multilayer hinged structures with initial strains. *J. Appl. Phys.* **94**, 5333–5336 (2003).
- Z. Chen, G. Huang, I. Trase, X. Han, Y. Mei, Mechanical self-assembly of a strain-engineered flexible layer: Wrinkling, rolling, and twisting. *Phys. Rev. Appl.* **5**, 17001 (2016).
- G. Huang, Y. Mei, Thinning and shaping solid films into functional and integrative nanomembranes. *Adv. Mater.* **24**, 2517–2546 (2012).
- R. Delmelle, B. Amin-Ahmadi, M. Sinnaeve, H. Idrissi, T. Pardoën, D. Schryvers, J. Proost, Effect of structural defects on the hydriding kinetics of nanocrystalline Pd thin films. *Int. J. Hydrogen Energy* **40**, 7335–7347 (2015).
- E. Lee, J. M. Lee, J. H. Koo, W. Lee, T. Lee, Hysteresis behavior of electrical resistance in Pd thin films during the process of absorption and desorption of hydrogen gas. *Int. J. Hydrogen Energy* **35**, 6984–6991 (2010).
- T. Hübert, L. Boon-Brett, G. Black, U. Banach, Hydrogen sensors – A review. *Sens. Actuators B Chem.* **157**, 329–352 (2011).

40. H.-X. Ji, X.-L. Wu, L.-Z. Fan, C. Krien, I. Fiering, Y.-G. Guo, Y. Mei, O. G. Schmidt, Self-wound composite nanomembranes as electrode materials for lithium ion batteries. *Adv. Mater.* **22**, 4591–4595 (2010).

Acknowledgments: Part of the experimental work was carried out in Fudan Nanofabrication Laboratory. **Funding:** This work was supported by the Natural Science Foundation of China (51322201, 51711540298, and U1632115), the Science and Technology Commission of Shanghai Municipality (14JC1400200), the National Key Technologies R&D Program of China (2015ZX02102-003), and the Changjiang Young Scholars Program of China. This work was also supported by the Priority Research Centers Program (2012-0006689) through the National Research Foundation (NRF) of Korea funded by the Ministry of Education, Science and Technology. We gratefully acknowledge partial support from the NRF of Korea (NRF-2017K2A9A2A06013377 and NRF-2017M3A7B4049466). Y.M. thanks the support from the Science and Technology Commission of Shanghai Municipality (17JC140170). **Author contributions:** B.X., T.L., and Y.M. designed this study. B.X. and J.W. fabricated and characterized the devices. B.X. and H.H. established the hydrogen testing system and

measured the actuating properties. B.X. and Z.T. calculated and simulated the actuating behavior. B.X., J.W., T.L., and Y.M. discussed and analyzed the results. B.X. and Y.M. wrote the paper. **Competing interests:** The authors declare that they have no competing interests. **Data and materials availability:** All data needed to evaluate the conclusions in the paper are present in the paper and/or the Supplementary Materials. Additional data related to this paper may be requested from the authors.

Submitted 30 August 2017

Accepted 15 February 2018

Published 6 April 2018

10.1126/sciadv.aap8203

Citation: B. Xu, Z. Tian, J. Wang, H. Han, T. Lee, Y. Mei, Stimuli-responsive and on-chip nanomembrane micro-rolls for enhanced macroscopic visual hydrogen detection. *Sci. Adv.* **4**, eaap8203 (2018).

Stimuli-responsive and on-chip nanomembrane micro-rolls for enhanced macroscopic visual hydrogen detection

Borui Xu, Ziao Tian, Jiao Wang, Heetak Han, Taeyoon Lee and Yongfeng Mei

Sci Adv 4 (4), eaap8203.
DOI: 10.1126/sciadv.aap8203

ARTICLE TOOLS	http://advances.sciencemag.org/content/4/4/eaap8203
SUPPLEMENTARY MATERIALS	http://advances.sciencemag.org/content/suppl/2018/04/02/4.4.eaap8203.DC1
REFERENCES	This article cites 40 articles, 6 of which you can access for free http://advances.sciencemag.org/content/4/4/eaap8203#BIBL
PERMISSIONS	http://www.sciencemag.org/help/reprints-and-permissions

Use of this article is subject to the [Terms of Service](#)

Science Advances (ISSN 2375-2548) is published by the American Association for the Advancement of Science, 1200 New York Avenue NW, Washington, DC 20005. 2017 © The Authors, some rights reserved; exclusive licensee American Association for the Advancement of Science. No claim to original U.S. Government Works. The title *Science Advances* is a registered trademark of AAAS.